The Astrophysical Journal, 1004:194 (14pp), 2026 June 20 https://doi.org/10.3847/1538-4357/ae5bad

ALMA Observations of [O I] 145 μm and [N II] 205 μm Emission Lines from Star-forming Galaxies at $z \sim 7$

Yoshinobu Fudamoto[1,2,3], Akio K. Inoue[2,4], Rychard Bouwens[5], Hanae Inami[6], Renske Smit[7], Daniel P. Stark[8], Manuel Aravena[9,10], Andrea Pallottini[11], Takuya Hashimoto[12,13], Masamune Oguri[1], Hiddo Algera[14], Rebecca A. A. Bowler[15], Elisabete da Cunha[16,17], Pratika Dayal[18], Andrea Ferrara[11], Seiji Fujimoto[19], Kasper E. Heintz[20,21], Alexander P. S. Hygate[5], Ivana F. van Leeuwen[5], Ilse De Looze[22], Lucie E. Rowland[23], Mauro Stefanon[24,25], Yuma Sugahara[2,3], Joris Witstok[26,27], and Paul P. van der Werf[23]

[1] Center for Frontier Science, Chiba University, 1-33 Yayoi-cho, Inage-ku, Chiba 263-8522, Japan; y.fudamoto@chiba-u.jp
[2] Waseda Research Institute for Science and Engineering, Faculty of Science and Engineering, Waseda University, 3-4-1 Okubo, Shinjuku, Tokyo 169-8555, Japan
[3] National Astronomical Observatory of Japan, 2-21-1, Osawa, Mitaka, Tokyo, Japan
[4] Department of Physics, School of Advanced Science and Engineering, Faculty of Science and Engineering, Waseda University, 3-4-1, Okubo, Shinjuku, Tokyo 169-8555, Japan
[5] Leiden Observatory, Leiden University, NL-2300 RA Leiden, The Netherlands
[6] Hiroshima Astrophysical Science Center, Hiroshima University, 1-3-1 Kagamiyama, Higashi-Hiroshima, Hiroshima 739-8526, Japan
[7] Astrophysics Research Institute, Liverpool John Moores University, 146 Brownlow Hill, Liverpool L3 5RF, UK
[8] Steward Observatory, University of Arizona, 933 N Cherry Ave, Tucson, AZ 85721, USA
[9] Instituto de Estudios Astrofísicos, Facultad de Ingeniería y Ciencias, Universidad Diego Portales, Av. Ejército 441, Santiago, Chile
[10] Millenium Nucleus for Galaxies (MINGAL), Chile
[11] Scuola Normale Superiore, Piazza dei Cavalieri 7, 56126 Pisa, Italy
[12] Division of Physics, Faculty of Pure and Applied Sciences, University of Tsukuba, Tsukuba, Ibaraki 305-8571, Japan
[13] Tomonaga Center for the History of the Universe (TCHoU), Faculty of Pure and Applied Sciences, University of Tsukuba, Tsukuba, Ibaraki 305-8571, Japan
[14] Institute of Astronomy and Astrophysics, Academia Sinica, 11F of Astronomy-Mathematics Building, No.1, Sec. 4, Roosevelt Rd, Taipei 106216, Taiwan, ROC.
[15] Jodrell Bank Centre for Astrophysics, Department of Physics and Astronomy, School of Natural Sciences, The University of Manchester, Manchester, M13 9PL, UK
[16] International Centre for Radio Astronomy Research, University of Western Australia, 35 Stirling Hwy, Crawley, WA 6009, Australia
[17] ARC Centre of Excellence for All Sky Astrophysics in 3 Dimensions (ASTRO 3D), Australia
[18] Kapteyn Astronomical Institute, University of Groningen, P.O. Box 800, 9700 AV Groningen, The Netherlands
[19] Department of Astronomy, The University of Texas at Austin, Austin, TX 78712, USA
[20] Cosmic Dawn Center (DAWN), Denmark
[21] Niels Bohr Institute, University of Copenhagen, Jagtvej 128, 2200 Copenhagen N, Denmark
[22] Sterrenkundig Observatorium, Ghent University, Krijgslaan 281 - S9, B-9000 Gent, Belgium
[23] Leiden Observatory, Leiden University, P.O. Box 9513, 2300 RA Leiden, The Netherlands
[24] Departament d'Astronomia i Astrofísica, Universitat de València, C. Dr. Moliner 50, E-46100 Burjassot, València, Spain
[25] Unidad Asociada CSIC "Grupo de Astrofísica Extragaláctica y Cosmología" (Instituto de Física de Cantabria—Universitat de València), Spain
[26] Kavli Institute for Cosmology, University of Cambridge, Madingley Road, Cambridge, CB3 0HA, UK
[27] Cavendish Laboratory, University of Cambridge, 19 JJ Thomson Avenue, Cambridge, CB3 0HE, UK
Received 2024 June 23; revised 2026 March 31; accepted 2026 April 4; published 2026 June 15

Abstract

We present results of new observations of [O I] 145 μm and [N II] 205 μm emission lines from four star-forming galaxies at redshifts between $z = 6.58$ and 7.68 that have previous detections of [C II] 158 μm and dust continua. Using the Atacama Large Millimeter/submillimeter Array, we successfully detect [O I] 145 μm emission from all targets at $>4\sigma$ significance. However, [N II] 205 μm emission is undetected in all galaxies (signal-to-noise ratio $< 3.5\sigma$) except for a tentative detection from A1689-zD1. From the observed high [C II]/[N II] emission line ratios ($\gtrsim$20−80), we find that most of the [C II] 158 μm emission arises from neutral gas regions (3σ lower limits of $\gtrsim$74%−96%). From [O I] 145 μm, [C II] 158 μm lines, and IR luminosities, we estimate the neutral gas densities of $n_{\rm H} = 10^{3.5}$–10^{6} cm^{-3} and the far-UV (FUV) radiation strengths of $G_0 \sim 10^{2.5}$–10^{3}. While the neutral gas densities are similar to those of high-redshift starburst galaxies, the FUV strengths are lower compared to both local and high-redshift starbursts. Finally, we estimate atomic hydrogen masses using [O I] 145 μm emission lines and the oxygen abundances measured from recent JWST observations. We find gas mass ratios of $f_{\rm gas} \sim 0.3$–0.8, which are similar to earlier studies using [C II] 158 μm. Starting from this pilot observation, future large [O I] 145 μm emission line surveys will provide us with currently little-known neutral gas properties of star-forming galaxies in the early Universe.

Unified Astronomy Thesaurus concepts: High-redshift galaxies (734); Galaxy formation (595); Galaxy evolution (594)

1. Introduction

Studying how star-forming galaxies evolved in the epoch of reionization (EoR; e.g., at $z > 6$) has crucial implications for our understanding of the cosmic reionization (e.g., P. Dayal & A. Ferrara 2018; B. E. Robertson 2022) as well as for our understanding of galaxy evolution in the later epochs (e.g.,

P. Madau & M. Dickinson 2014). Deep observations using the Hubble Space Telescope, the recent observations using the James Webb Space Telescope (JWST), and several ground-based optical/near-IR facilities have completely revolutionized our view of galaxy evolution in the high-redshift Universe through their extremely high sensitivity and high resolution in the rest-frame UV extremely and/or optical wavelengths (e.g., R. J. Bouwens et al. 2015; P. A. Oesch et al. 2018; R. P. Naidu et al. 2022; A. J. Cameron et al. 2023; S. L. Finkelstein et al. 2023; S. Fujimoto et al. 2023; Y. Harikane et al. 2023; P. A. Oesch et al. 2023; M. J. Rieke et al. 2023; B. Robertson et al. 2024; C. C. Williams et al. 2024; S. Carniani et al. 2024; B. Wang et al. 2024). While these rest-frame UV/optical observations enabled access to the galaxies' star formation activities through the observations of ionized gas, the cold neutral and the molecular gas—the direct fuel for star formation activities—is challenging to probe in emission at the rest-frame UV/optical wavelengths. This is because key emission used to trace neutral gas for relatively lower-redshift galaxies, such as molecular gas (e.g., P. M. Solomon & P. A. Vanden Bout 2005), neutral atomic gas emission (e.g., F. Walter et al. 2011), and dust continuum (e.g., N. Scoville et al. 2016), exist mostly at far-IR (FIR) wavelength range (however, see, e.g., K. E. Heintz et al. 2024 for probing the neutral gas in absorption).

The unprecedented sensitivity and high spatial resolution of the Atacama Large Millimeter/submillimeter Array (ALMA) have largely improved studies of galaxy formation and evolution by enabling the probe of dust continuum and emission lines in the FIR wavelength from galaxies in the EoR (see J. A. Hodge & E. da Cunha 2020 for a review). In particular, recent ALMA observations detected [C II] 158 μm emission lines from a statistically significant number of EoR galaxies (e.g., R. Smit et al. 2018; T. Hashimoto et al. 2019; S. Carniani et al. 2020; R. J. Bouwens et al. 2022; Y. H. V. Wong et al. 2022; S. Fujimoto et al. 2024; K. E. Heintz et al. 2023a; S. Schouws et al. 2023; R. Fernández Aranda et al. 2024). Observations of the [C II] emission line and studies of the interstellar medium (ISM) by combining multiple emission lines provide crucial diagnostics for the physical properties and galaxies' star formation rates (SFRs; e.g., Y. Harikane et al. 2020; D. Schaerer et al. 2020; L. Vallini et al. 2021; Y. Sugahara et al. 2022; S. Schouws et al. 2022; J. Witstok et al. 2022; H. S. B. Algera et al. 2023; M. Killi et al. 2023; L. Vallini et al. 2024). However, multiple FIR emission line observations of high-redshift galaxies are limited to extremely IR luminous galaxies such as gravitationally lensed dusty star-forming galaxies, QSO host galaxies, submillimeter galaxies (SMGs; e.g., C. De Breuck et al. 2019; R. A. Meyer et al. 2022), and less extreme star-forming high-redshift galaxies, previously inaccessible without the aid of gravitational lensing, have not been well studied.

First, we examine the fraction of [C II] 158 μm originating from either ionized gas or neutral gas (both atomic and molecular) using observations of the [N II] 205 μm emission line. C^+ ions exist in both ionized and neutral gas because their ionization potential is 11.3 eV, while N^+ is found only in ionized gas due to its higher ionization potential of 14.5 eV, which exceeds that of hydrogen. Because [N II] 205 μm and [C II] 158 μm have similar critical densities ($n_{\rm crit} \sim 40\,{\rm cm}^{-3}$ and $n_{\rm crit} \sim 50\,{\rm cm}^{-3}$ with electrons, respectively) and excitation potentials (70 K for [N II] 205 μm and 91 K for [C II] 158 μm), both lines are produced in similar physical conditions inside ionized gas clouds. Thus, the line ratio between [C II] 158 μm and [N II] 205 μm for the ionized region can be estimated based on their assumed abundance and emissivity, and the excess [C II] 158 μm luminosity would originate from neutral gas.

As several previous studies performed for local and high-redshift IR luminous galaxies, the luminosity ratio between [N II] 205 μm and [C II] 158 μm indeed works as an indicator for constraining the origin of [C II] 158 μm emission line for low- and high-redshift star-forming galaxies (S. Malhotra et al. 2001; T. E. Oberst et al. 2011; R. Decarli et al. 2014; M. Béthermin et al. 2016; R. Pavesi et al. 2016; K. V. Croxall et al. 2017; M. M. Lee et al. 2021; A. Pensabene et al. 2021; J. Witstok et al. 2022; R. Decarli et al. 2023).

Second, we investigate the properties of the warm neutral star-forming gas traced by the [O I] 145 μm emission. Neutral oxygen (O^0) has a slightly higher ionization potential than hydrogen (13.62 eV), and therefore coexists with neutral atomic hydrogen regions such as photodissociation regions (PDRs) and the warm neutral medium (C. F. McKee & J. P. Ostriker 1977), until it is mostly depleted into molecules (e.g., CO or H_2O). O^0 is also expected to exist within H_2 molecular regions, especially in low metallically "CO-dark" molecular gas environments such as those in high-redshift galaxies (e.g., S. C. Madden et al. 2020). The [O I] 145 μm emission line ($\lambda_{\rm rest} = 145.53\,\mu$m) is one of the important coolants, tracing relatively dense gas owing to its high critical density, $n_{\rm crit}^{\rm H} \sim 10^5\,{\rm cm}^{-3}$, and being generally optically thin, unlike the [O I] 63 μm transition (e.g., A. G. G. M. Tielens & D. Hollenbach 1985; M. J. Kaufman et al. 1999). Based on the wealth of the knowledge constructed in theoretical and observations understanding (M. G. Wolfire et al. 1990; G. J. Ferland et al. 1998; D. J. Hollenbach & A. G. G. M. Tielens 1999; D. E. Osterbrock & G. J. Ferland 2006), recent observational studies started to provide first constraints of these ISM parameters of high-redshift galaxies, which is crucial step for early galaxy studies as previously only a few lines (only [C II] lines in most cases) are accessible. Recently, the [O I] 145 μm line has been observed in the local dwarf galaxies, which would work as analogs of high-redshift galaxies (e.g., D. Cormier et al. 2015; V. Lebouteiller et al. 2019; S. C. Madden et al. 2020; D. A. Hunter et al. 2024) as well as from high-redshift starbursts and active galactic nuclei (C. De Breuck et al. 2019; J. Yang et al. 2019; M. Novak et al. 2020; M. M. Lee et al. 2021; A. Pensabene et al. 2021; R. A. Meyer et al. 2022; K. C. Litke et al. 2023). These studies attempt to derive key parameters, such as neutral gas density (n) and far-UV radiation field (G_0), of the PDRs to molecular gas surface layers using combinations of [C II] 158 μm, [O I] 145 μm, and other FIR lines (e.g., [C I] and CO lines). While several studies have highlighted the importance of obtaining [O I] 145 μm emission lines in high-redshift SMGs and QSO hosts due to their brightness and accessibility (e.g., C. De Breuck et al. 2019; M. M. Lee et al. 2021; R. A. Meyer et al. 2022), no observations of [O I] have been performed for a less extreme galaxy population in the EoR. In this study, we present the analyses and results of the first pilot observations for the [O I] 145 μm emission lines in [C II] bright star-forming galaxies in the EoR.

This paper is organized as follows. In Section 2, we describe our target galaxies and the ALMA observations used in this

Table 1
List of the Target Galaxies in this Study, Ordered by Their Redshifts

Source	α_{J2000} (deg)	δ_{J2000} (deg)	z_{spec}	Magnification (μ)	L_{UV} ($10^{11}\,L_{\odot}$)	M_* ($10^9\,M_{\odot}$)	SFR ($M_{\odot}$ yr^{-1})
REBELS-38	150.725208	2.703333	6.577	⋯	1.2 ± 0.3	$3.8^{+1.7}_{-3.6}$	116 ± 45
A1689-zD1	197.874708	−1.321861	7.132	4.14 ± 0.36	0.63 ± 0.05[a]	$3.7^{+1.6}_{-1.1}$[a]	83 ± 8[a]
REBELS-25	150.134667	1.742028	7.307	⋯	1.0 ± 0.2	$7.7^{+3.2}_{-2.6}$	200 ± 83
REBELS-18	149.449583	2.345472	7.675	⋯	1.5 ± 0.2	$3.1^{+8.1}_{-2.5}$	72 ± 20

Notes. Properties for REBELS-38, REBELS-25, and REBELS-18 are adopted from R. J. Bouwens et al. (2022) and S. Schouws et al. (2026, in preparation), and A1689-zD1 are presented in L. D. Bradley et al. (2008), D. Watson et al. (2015), A. K. Inoue et al. (2020), and T. J. L. C. Bakx et al. (2021). Magnification of A1689-zD1 is newly updated in this study (see Appendix A).
(see Appendix A).
[a] Values are corrected by scaling with the updated gravitational lensing magnification factor of $\mu = 4.14$.

Table 2
Summary of ALMA Observations Presented in This Work

Source	Emission Line	t_{int} (hr)	PVW (mm)	Beam FWHM	rms$_{cont.}$ (μJy beam^{-1})	rms$_{line, 25\,km\,s^{-1}}$ (mJy beam^{-1})	ALMA project ID
REBELS-38	[N II] 205 μm	1.5	0.749	1″2 × 0″9	11	0.17	#2022.1.01384.S
	[O I] 145 μm	1.2	0.322	1″3 × 1″0	11	0.24	#2022.1.00446.S
A1689-zD1	[N II] 205 μm[a]	2.3	0.503	1″5 × 1″2	6.5	0.10	#2021.1.00247.S
	[O I] 145 μm	0.2	0.587	1″3 × 1″0	25	0.44	#2022.1.00446.S
REBELS-25	[N II] 205 μm	1.5	0.682	1″5 × 1″0	8.8	0.28	#2022.1.01384.S
	[O I] 145 μm	0.8	1.470	0″6 × 0″5	14	0.27	#2022.1.00999.S
REBELS-18	[O I] 145 μm	2.6	0.352	1″3 × 1″2	6.5	0.12	#2022.1.00446.S

Note.
[a] [N II] 205 μm observation of A1689-zD1 is further presented and discussed in detail in S. Fujimoto et al. (2026, in preparation).

study. In Section 3, we present our data analysis and measurements for the [O I] 145 μm and [N II] 205 μm emission lines. In Section 4, we present the results of the study. In Section 5, we compare to previous studies and discuss our results. Finally, we conclude with the summary in Section 6. Throughout this paper, we assume a cosmology with $(\Omega_m, \Omega_\Lambda, h) = (0.3, 0.7, 0.7)$, and the G. Chabrier 2003 initial mass function (IMF) with stellar masses ranging from 0.1 to 300 $M_{\odot}$, where applicable.

2. Observation

2.1. Target Galaxies

Table 1 summarizes our target galaxies and their basic properties. Below, we detail our sample selection criteria.

Our targets are star-forming galaxies at $z > 6.5$. SFRs of the targets are ∼2× −∼4× higher than those of the main-sequence galaxies at the same redshift (C. Schreiber et al. 2015; M. W. Topping et al. 2022). Although these SFRs are still higher than the main-sequence galaxies at this redshift, they are comparable to those of previously studied systems. In particular, the SPT0418-47 system, based on updated measurements and gravitational magnification corrections, has an SFR of $\gtrsim$150 $M_{\odot}$ yr^{-1} (B. Peng et al. 2023; J. Cathey et al. 2024), and may be one of the very few high-redshift star-forming galaxies with multiple FIR line measurements at similar stellar mass and SFR (C. De Breuck et al. 2019). To select targets, we searched all previous [C II] emission line observations, including the Cycle-7 ALMA large program Reionization Era Bright Emission Line Survey (REBELS; R. J. Bouwens et al. 2022) as well as previously published [C II] emission line observations (R. Smit et al. 2018; T. Hashimoto et al. 2019; S. Carniani et al. 2020; H. B. Akins et al. 2022; S. Schouws et al. 2022, 2025). Individual studies have their own selection methods based on the estimated accuracy of photometric redshifts as well as based on detections of Lyα emission lines. However, these galaxies were originally all selected based on their bright rest-frame UV luminosities (typically $M_{UV} < -21$ mag; R. J. Bouwens et al. 2022).

We further selected galaxies based on their expected luminosities of [O I] 145 μm and [N II] 205 μm emission based on previously detected [C II] 158 μm line emission luminosities. In particular, we performed flux-limited selection of galaxies with their apparent [C II] luminosity of $L_{[C\,II]} > 1.1 \times 10^9\,L_{\odot}$. Using these criteria, we selected four [C II] luminous star-forming galaxies; REBELS-38 at $z = 6.577$ (R. J. Bouwens et al. 2022; H. S. B. Algera et al. 2023), A1689-zD1 at $z = 7.132$ (e.g., D. Watson et al. 2015; T. J. L. C. Bakx et al. 2021; H. B. Akins et al. 2022; M. Killi et al. 2023), REBELS-25 at $z = 7.307$ (R. J. Bouwens et al. 2022; H. S. B. Algera et al. 2023; A. P. S. Hygate et al. 2023; L. E. Rowland et al. 2024), and REBELS-18 at $z = 7.675$ (R. J. Bouwens et al. 2022).

2.2. ALMA Observations

Observation conditions, integration times, and beam sizes of these observations are summarized in Table 2. In the following, we present details of these observations.

2.2.1. [O I] 145 μm and [N II] 205 μm Emission Line

Observations of [O I] 145 μm emission lines of target galaxies were newly performed during ALMA Cycle-9

#2022.1.00446.S (PI: Fudamoto) and #2022.1.00999.S (PI: De Looze). [N II] 205 μm emission lines were newly observed in Cycle-9 #2022.1.01384.S (PI: Fudamoto) for REBELS-38 and REBELS-25. [N II] 205 μm data of A1689-zD1 were retrieved from the ALMA archive #2021.1.00247.S (PI: Fujimoto). [N II] 205 μm emission line observations of REBELS-38 and A1689-zD1 were fully executed. On the other hand, [N II] 205 μm observations of REBELS-25 were only partially performed.

2.3. ALMA Data Reduction

In this study, we present newly obtained ALMA data for the [O I] and [N II] emission lines from the target galaxies. [C II] 158 μm and [O III] 88 μm emission line data are adopted from D. Watson et al. (2015), H. B. Akins et al. (2022), R. J. Bouwens et al. (2022), M. Killi et al. (2023), B. Wang et al. (2024), and H. S. B. Algera et al. (2024).

The observed ALMA data of [O I] 145 μm and [N II] 205 μm were reduced and analyzed using the Common Astronomy Software Application (CASA) version 6.2.1 (The CASA Team et al. 2022). ALMA observations for [O I] 145 μm and [N II] 205 μm emission lines were calibrated using the second-stage quality assurance pipeline codes (i.e., SCRIPTFORPI.PY) without further flagging and editing.

To examine and analyze emission lines, we created data cubes using spectral windows (SPWs) that include the sky frequencies of each emission line, accounting for the target's spectroscopic redshift. To create data cubes using TCLEAN of CASA, we applied a fixed velocity channel binning of 25 km s^{-1} for all data cubes. Rest-frame frequencies of each data cube were set to the sky frequency of each emission line observation based on the [C II] emission line detections (Table 3). Underlying dust continua of the target galaxies were subtracted using the CASA task UVCONTSUB by fitting flat continua for the SPWs that do not include emission lines. Dust continuum maps of all observations were made using the continuum SPWs, using the TCLEAN task of CASA, and using the multifrequency synthesis imaging mode.

When we created data cubes and dust continuum maps, we performed synthesized beam deconvolutions using TCLEAN by setting stopping thresholds to be 3× the pixel-by-pixel rms of the dirty images and by setting the maximum number of iterations to 500. For data cubes, the background rms was calculated as the average of the rms of all channels. The threshold and parameters did not affect final data quality, as there were no particular bright sources in the targeted fields. All data cubes and continuum maps were imaged using the NATURAL weighting scheme to maximize point source sensitivity. The achieved sensitivity of pixel-by-pixel rms of the cleaned cubes and continuum maps is presented in Table 2.

3. Analysis

3.1. Emission Line Detections

For the [O I] 145 μm emission line data, we find clear detections of emission lines at the expected frequencies from all targets. For the detected [O I] lines, we created moment-0 images by determining the appropriate frequency widths that capture [O I] 145 μm emission using an iterative method. First, we performed 1D Gaussian fits on the extracted spectra and reintegrated the data cube using frequency ranges that encompass the 2σ line widths. Next, we reextracted spectra from regions in the moment-0 images where pixel values exceeded 2 σ, further refining the emission line spectra. We then repeated the 1D Gaussian fitting to update the frequency width and generate new moment-0 images. This process was repeated until the selected channels for moment-0 image creation converged.

For the [N II] 205 μm emission line data of REBELS-38 and REBELS-25, we did not identify any emission lines from the extracted spectra. To further examine the [N II] lines, we created moment-0 images by using velocity widths fixed to those of [C II] 158 μm emission lines (1× FWHMs and 2× FWHMs). We only found signals $\lesssim 3\sigma$ at the expected source position. We thus concluded that all the [N II] 205 μm emission lines were nondetected.

For [N II] 205 μm emission line of A1689-zD1, we found a weak $\lesssim 3\sigma$ signal in its moment-0 map integrated over the same velocity FWHM as the [C II] 158 μm emission line (Y. H. V. Wong et al. 2022). However, we treated the [N II] 205 μm of A1689-zD1 as an upper limit based on the following reasons. In the spectra (bottom panels in Figure 1), the positive signal has two peaks that are slightly off from the expected frequency from the [C II] emission detection. As clumpy structures of A1689-zD1 were reported by Y. H. V. Wong et al. (2022), and the spectra have a non-Gaussian shape, the positive signal might arise from some of the clumps distributed in a line of sight in the A1689-zD1 and the [N II] emitting region, which do not overlap with that of [C II] emission line. As our current observations of [N II] 205 μm and [O I] 145 μm do not have enough spatial resolution to resolve the clumps and as the detection signals are marginal, we treat the [N II] 205 μm signal of A1689-zD1 as an upper limit. However, even if we treat the [N II] 205 μm as detection, our results do not change.

We measured line fluxes (for the detected lines) and flux upper limits (for nondetections) using the moment-0 images. For the detected [O I] 145 μm emission lines, we performed 2D Gaussian fittings using the CASA task IMFIT. For nondetected [N II] 205 μm emission lines, we measured 3σ upper limit fluxes by calculating the 3× pixel-by-pixel rms of moment-0 maps integrated over the FWHMs of [C II] emission lines. All emission line images are shown in Figure 1, and our ALMA measurements are listed in Table 3.

3.2. Dust Continuum Detection

Dust continua were all clearly detected from all targets with >4.5σ significance at the source positions. We measured continuum fluxes by 2D Gaussian fittings using the CASA task IMFIT. Measured continuum fluxes are listed in Table 3. Appendix B shows dust continuum images.

4. Results

Here we present the results of our observations, with particular focus on the inferred FIR line luminosities and the physics implied by their intrinsic ratios.

4.1. IR Luminosity and FIR Spectral Energy Distribution

The FIR spectral energy distribution (SED) and IR luminosities[28] of A1689-zD1 and REBELS-25, REBELS-38

[28] Throughout this work, L_{IR} are calculated using the rest-frame wavelength range of 8−1000 μm.

Table 3
Summary of Measurements of Our Samples

Name	REBELS-38	A1689-zD1	REBELS-25	REBELS-18
Magnification factor	⋯	4.14 ± 0.36[a]	⋯	⋯
$z_{[O\ III]88}$	⋯	7.132 (a)	7.3052 ± 0.0004 (i)	⋯
$FWHM_{[O\ III]88}$ (km s^{-1})	⋯	182 ± 31 (a)	203 ± 38 (i)	⋯
$f_{[O\ III]88}$ (Jy km s^{-1})	⋯	5.75 ± 0.38 (b)	$0.90^{+0.23}_{-0.21}$ (i)	⋯
$L_{[O\ III]88}$ ($\times 10^8\ L_\odot$)	⋯	124 ± 8 (b)	$20.0^{+5.1}_{-4.6}$ (i)	⋯
S_{88} (μJy)	334 ± 63 (e)	1760 ± 280 (f)	490 ± 120 (e)	⋯
$z_{[C\ II]158}$	6.5770 ± 0.0001	7.132(a)	7.3065 ± 0.0002	7.6750 ± 0.0001
$FWHM_{[C\ II]158}$ (km s^{-1})	204 ± 13	323 ± 8(c)	322 ± 12	209 ± 11
$f_{[C\ II]158}$ (Jy km s^{-})	1.58 ± 0.12	3.56 ± 0.07(b)	1.28 ± 0.04	0.81 ± 0.05
$L_{[C\ II]158}$ ($\times 10^8\ L_\odot$)	16.8 ± 1.6	45.0 ± 1. 0 (b)	15.9 ± 1.0	10.8 ± 0.9
S_{158} (μJy)	163 ± 23[d]	558 ± 102 (g)	260 ± 22d	53 ± 10 (d)
T_d (K)	46^{+18}_{-11} (j)	42^{+13}_{-7} (h)	32^{+9}_{-7} (i)	39^{+12}_{-7} (j)
β_d	...	$1.61^{+0.60}_{-0.75}$ (e)	2.5 ± 0.4 (i)	...
L_{IR} ($\times 10^{11}\ L_\odot$)	$8.0^{+4.4}_{-2.9}$	20.1 ± 0.7 (a)	$5.0^{+2.9}_{-1.0}$ (i)	$3.5^{+2.0}_{-1.3}$
This Work				
$z_{[O\ I]145}$	6.5774 ± 0.0003	7.134 ± 0.0006	7.308 ± 0.001	7.676 ± 0.0006
$FWHM_{[O\ I]145}$ (km s^{-1})	112 ± 24	278 ± 51	440 ± 95	165 ± 38
$f_{[O\ I]145}$ (Jy km s^{-1})	0.110 ± 0.022	0.556 ± 0.137	0.394 ± 0.082	0.107 ± 0.028
$L_{[O\ I]145}$ ($\times 10^8\ L_\odot$)	1.3 ± 0.3	7.3 ± 1.8	5.3 ± 1.1	1.6 ± 0.4
S_{145} (μJy)	220 ± 28	705 ± 76	270 ± 41	116 ± 12
$f_{[N\ II]205}$ (Jy km s^{-1})	<0.045 (3σ)	<0.059 (3σ)	<0.076 (3σ)	⋯
$L_{[N\ II]205}$ ($\times 10^8\ L_\odot$)	<0.37 (3σ)	<0.55 (3σ)	<0.73 (3σ)	⋯
S_{205} (μJy)	131 ± 39	269 ± 15	94 ± 12	⋯
$f^{PDR}_{[CII]}$	>0.92	>0.96	>0.83	⋯

Note.
[a] See Appendix A for the discussion of the magnification factor. All the measurements from A1689-zD1 are not corrected for the lensing magnification.
Refrences. (a) H. B. Akins et al. (2022), (b) M. Killi et al. (2023), (c) Y. H. V. Wong et al. (2022), (d) H. Inami et al. (2022), (e) H. S. B. Algera et al. (2023), (f) A. K. Inoue et al. (2020), (g) D. Watson et al. (2015). (h) T. J. L. C. Bakx et al. (2021), (i) H. S. B. Algera et al. (2024). (j) L. Sommovigo et al. (2022).

have already been studied in detail by T. J. L. C. Bakx et al. (2021) and H. S. B. Algera et al. (2023). We adopt dust temperatures (T_d), emissivity indexes (β_d), and IR luminosities (L_{IR}) measured in these previous studies.

REBELS-18 does not have direct FIR SED measurements, as only low-spatial resolution $\lambda = 158\ \mu$m continuum observations were obtained so far. With the new $\lambda = 145$ and 205 μm continuum observations, the dust temperatures are challenging to constrain as these wavelengths only cover the Rayleigh–Jeans tail of the emission, and the accurate constraints of dust temperatures require higher frequency (e.g., $\lambda_{rest} \lesssim 100\ \mu$m; A. L. Faisst et al. 2020) or higher spatial resolution observations (e.g., A. K. Inoue et al. 2020; Y. Fudamoto et al. 2023). In this study, we rely on the dust temperature and IR luminosity estimations for REBELS-18 inferred from the [C II] emission lines (L. Sommovigo et al. 2022).

4.2. *[N II] 205 μm and [C II] 158 μm Line Luminosity Ratio*

Using the nondetections or tentative detections of the [N II] 205 μm emission lines for our target galaxies, we calculated 3 σ lower limit luminosity ratio $L_{[C\ II]158}/L_{[N\ II]205}$ ranging from $\gtrsim$21 to $\gtrsim$87 (left panel of Figure 2). The observed line ratios of these EoR star-forming galaxies are generally much higher than the average distributions of local IR luminous galaxies observed by GOALS (T. Díaz-Santos et al. 2017) and high-redshift SMGs at $z \sim 4$–6 (D. J. M. Cunningham et al. 2020). We will discuss the implications of these luminosity ratios in detail in Section 5.1.

4.3. *[O I] 145 μm, [C II] 158 μm, and [O III] 88 μm Line Luminosity Ratio*

From the observed [O I] 145 μm emission line luminosity, we measure the [O I] 145 μm to [C II] 158 μm emission line ratios to be in a range between 0.08 ± 0.02 and 0.33 ± 0.07 with a median of 0.16 (Figure 3). The range of the [O I]/[C II] ratio is similar to that of $z > 4$ QSOs/SMGs. When we compare the [O I]/[C II] ratio with local galaxies, most of our observation results are distributed around the higher edge of the local dwarf galaxy distribution at a fixed IR luminosity range. These relatively high [O I]/[C II] line ratios are seen in certain local environments, such as highly irradiated gas in ULIRGs (e.g., [O I]/[C II]∼0.1–1, N. P. Abel et al. 2009; J. Fischer et al. 2010), and in dense PDRs (e.g., T. G. Bisbas et al. 2021; M. W. Pound & M. G. Wolfire 2023 and see also Section 5.2.2). We will discuss the implications of these [O I] 145 μm observations in detail by comparing with the CLOUDY models in Section 5.2

We also investigated [C II] 158 μm/[O I] 145 μm luminosity ratio versus [O III] 88 μm/[O I] 145 μm luminosity ratio (right panel of Figure 3) for REBELS-25 and A1689-zD1, as these galaxies have [O III] 88 μm emission line observations

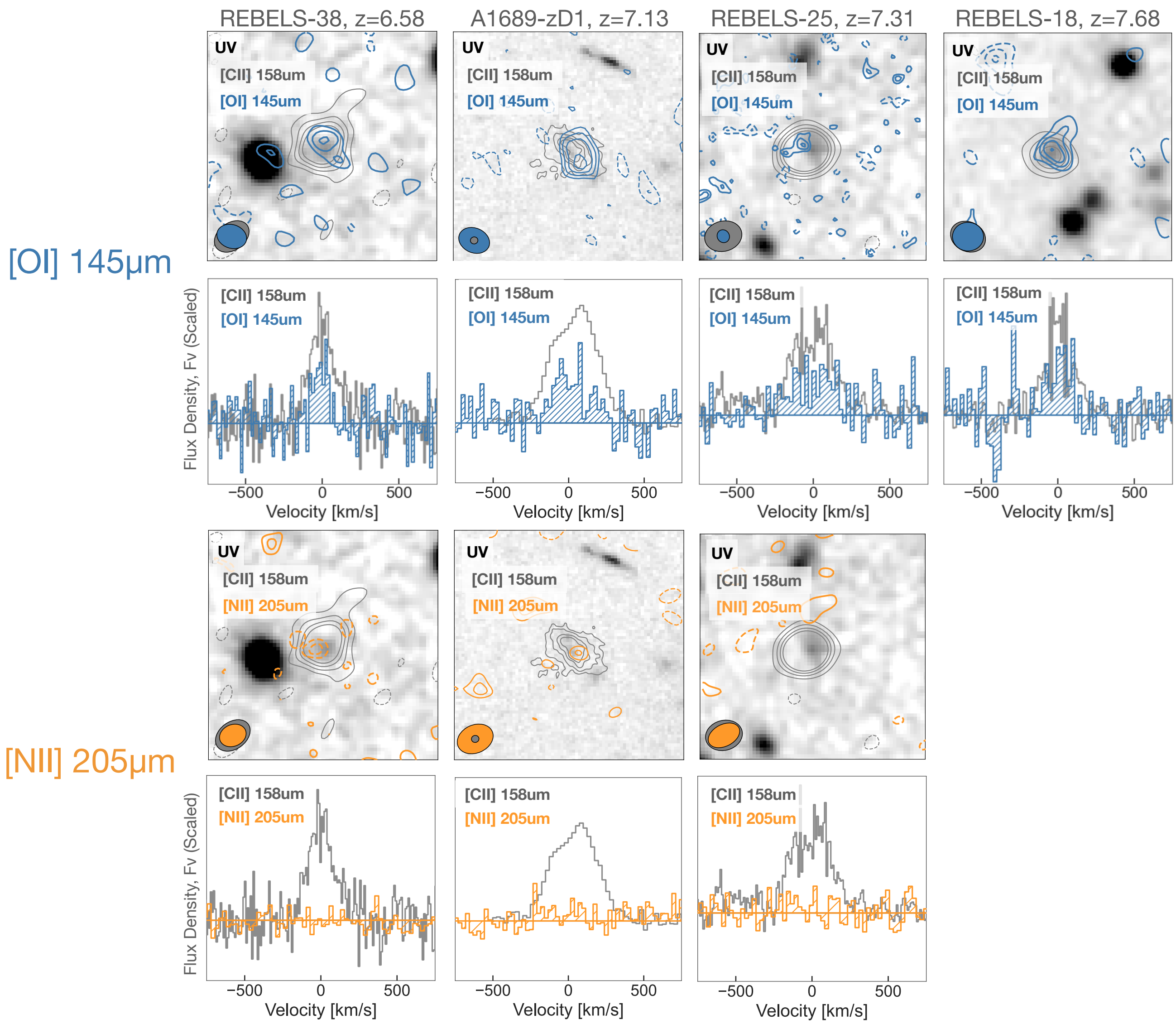

Figure 1. Cutouts and spectra of [C II] 158 μm, [O I] 145 μm, and [N II] 205 μm emission lines of the targets. For REBELS-38, REBELS-25, and REBELS-18, background images of cutouts show rest-frame UV continuum obtained by stacking *J*-, *H*-, and *K*-band images from the UVISTA survey (H. J. McCracken et al. 2012). For A1689-zD1, the Hubble Space Telescope F160W image is shown in the background of the cutouts. Cutouts in the upper panels: Gray and blue contours show moment-0 images of [C II] 158 μm and [O I] 145 μm emission lines, respectively. Cutouts in the lower panels: gray and orange contours show moment-0 images of [C II] 158 μm and [N II] 205 μm emission lines, respectively. For all cutouts, solid contours show 3, 5, 7, 9 σ for [C II] and 2, 3, 4, 5 σ for [O I] and [N II] data. Dashed contours show the −2, −3, −4, and −5σ signals (if they exist). *Spectra*: Gray histograms show [C II] 158 μm lines. Blue and orange hatched histograms show [O I] 145 μm and [N II] 205 μm lines. Flux densities of the spectra are scaled by arbitrary factors. While [O I] emission lines of all the targets are detected with the significance of $>4\sigma$, [N II] emission lines are nondetected except for the weak signal from A1689-zD1.

reported in previous studies. In this diagram, REBELS-25 is located at the lower left corner, i.e., the lowest ranges of [O III] 88 μm/[O I] 145 μm ratio as well as [C II] 158 μm/[O I] 145 μm ratio. In contrast, A1689-zD1 shows a higher [O III] 88 μm/[O I] 145 μm ratio compared to most local galaxies/active galactic nuclei (AGNs), similar to the local dwarf galaxies studied by D. Cormier et al. (2015). The [O III] 88 μm/[O I] 145 μm line ratio is correlated with the volume filling factor of ionized oxygen, which in turn is related to the ionization parameter ($U_{\rm ion;}$ C. De Breuck et al. 2019).

Previous studies have shown that the high [O III]/[C II] line ratio in high-redshift galaxies is due to a high $U_{\rm ion}$ and/or lower PDR covering factors (e.g., T. Hashimoto et al. 2019; Y. Harikane et al. 2020; J. Witstok et al. 2022). REBELS-25 and A1689-zD1 have [O III]/[C II] ratios of 1.3 (H. S. B. Algera et al. 2023) and 2.1 (Y. H. V. Wong et al. 2022), respectively. The [O III]/[C II] ratio of REBELS-25 is among the lowest values observed for $z > 6$ star-forming galaxies. The low [O III] 88 μm/[O I] 145 μm line ratio of REBELS-25, suggesting low $U_{\rm ion}$, is consistent with its relatively low [O III] 88 μm/[C II] 158 μm line ratio. In contrast, the higher [O III] 88 μm/[O I] 145 μm line ratio of A1689-zD1 suggests a higher $U_{\rm ion}$, which is generally consistent with its higher [O III] 88 μm/[C II] 158 μm ratio. Although the sample size is currently too small, these line ratios suggest the potential for using multiple FIR emission lines to diagnose gas properties.

4.4. Origin of [O I] and [C II] Emission Lines of REBELS-38

Most of the target galaxies have [O I] 145 μm emission lines that spatially coincide and have profiles consistent with those

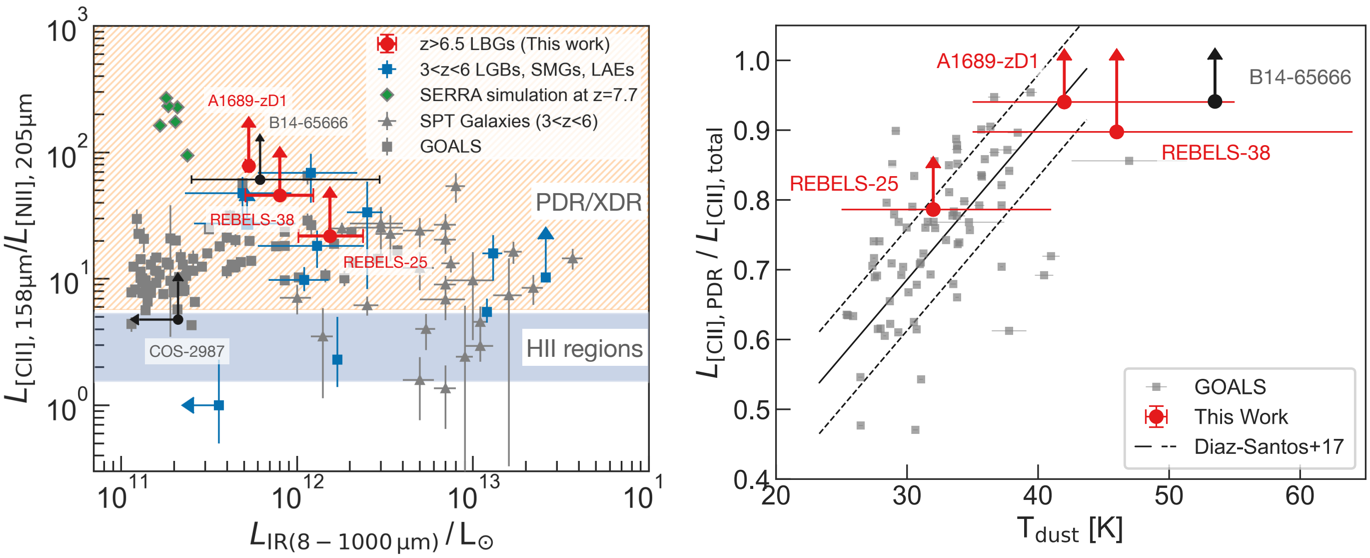

Figure 2. Left panel: [C II] 158 μm over [N II] 205 μm emission line luminosity ratio as a function of the IR luminosity of local and high-redshift galaxies. Local galaxies are obtained from the GOALS sample (T. Díaz-Santos et al. 2017), while high-redshift galaxies at $z \sim 3-6$ were studied in R. Decarli et al. (2014); R. Pavesi et al. (2019), D. J. M. Cunningham et al. (2020), A. Pensabene et al. (2021), C. Schreiber et al. (2021), J. Witstok et al. (2022), and in this work. The blue band represents [C II] 158 μm over [N II] 205 μm emission line ratios expected from H II regions with a wide parameter range, and the orange hatched band represents the line ratio from PDR or X-ray dominated region (J. Witstok et al. 2022). The 3 σ lower limits of the $z > 6.5$ galaxies (red points with arrows) are located well above most of the local and high-redshift galaxy distribution. The measured high ratios of [C II] 158 μm over [N II] 205 μm emission line luminosity suggest that the [C II] emission lines from the ISM of $z > 6.5$ galaxies are dominated by those from PDRs. Right panel: $f^{\rm PDR}_{\rm [CII]158}$ as a function of the dust temperatures ($T_{\rm d}$). Gray squares are $z \sim 0$ galaxies from GOALS (T. Díaz-Santos et al. 2017). The black solid line shows the correlation between $f^{\rm PDR}_{\rm [C\,II]158}$ and $T_{\rm d}$ found in T. Díaz-Santos et al. (2017). The 3 σ lower limits found in these studies are consistent with the $z \sim 0$ results, which reach temperatures of up to $T_{\rm d} \sim 40$ K.

of [C II] emission lines. However, the [O I] emission line of REBELS-38 has a noticeably narrower emission line profile compared with the [C II] emission line (i.e., $\mathrm{FWHM}_{\rm [O\,I]} = 112 \pm 24$ vs $\mathrm{FWHM}_{\rm [C\,II]} = 204 \pm 13\,\mathrm{km\,s^{-1}}$). While the currently measured difference is marginal ($\sim$2.5 σ), such a discrepancy, if confirmed, suggests that the [O I] and [C II] of REBELS-38 would originate from different ISM components. Because the present data are limited by both spatial resolution and sensitivity, follow-up observations of both [O I] and [C II] emission lines will be necessary to study this possibility in detail. Thus, we only remark on this potential issue for REBELS-38.

5. Discussion

5.1. Origins of [C II] 158 μm Emission Lines

The observations of [C II] and [N II] show that the target galaxies have a high luminosity ratio; $L_{\rm [C\,II]158}/L_{\rm [N\,II]205} \gtrsim 21$ to $\gtrsim 87$ (left panel of Figure 2). Previous studies (e.g., R. Decarli et al. 2023) show that the high $L_{\rm [C\,II]158}/L_{\rm [N\,II]205}$ indicates that the [C II] 158 μm emission lines are dominated by those from the PDR and not from H II regions.

Following these studies, we describe the fraction of [C II] 158 μm emission originated from PDR using [C II] and [N II] luminosity ratio as:

$$f^{\rm PDR}_{\rm [C\,II]} = 1 - R_{\rm ion}\left(\frac{L_{\rm [N\,II]205\,\mu m}}{L_{\rm [C\,II]158\,\mu m}}\right), \quad (1)$$

where $R_{\rm ion}$ is the expected [C II] over [N II] emission line luminosity ratio when [C II] is originating entirely from H II regions. Due to the similar emission properties of [C II] 158 μm and [N II] 205 μm (e.g., their critical density and excitation temperature), $R_{\rm ion}$ was found to have a tight range between 2.5 and 3, assuming an electron density of the range $n_{\rm e} = 10$–$100\,\mathrm{cm^{-3}}$ (K. V. Croxall et al. 2017). Using wider ranges of parameters (metallicity, ionization field strength, gas density), J. Witstok et al. (2022) found a wider range of $R_{\rm ion} = 1.5$–5.7 by incorporating various metallicities, ionization parameters, hydrogen densities, and elemental abundances (blue band in Figure 2). In this study, we use $R_{\rm ion} = 3.6$ as our fiducial value by taking an average of $R_{\rm ion}$ found in the analysis of J. Witstok et al. (2022). Later, we will discuss how the results change by using a higher value of $R_{\rm ion} = 5.7$.

With the measured luminosity ratio between [C II] 158 μm and [N II] 205 μm of the target galaxies, we find 3σ lower limits of $f^{\rm PDR}_{\rm [CII]} > 0.92$, > 0.96, and > 0.83 using $R_{\rm ion} = 3.6$ for REBELS-38, A1689-zD1, and REBELS-25, respectively. We also estimated the PDR fraction of [C II] of B14-65666 at $z = 7.15$, where [N II] 205 μm line luminosity is estimated from [N II]122 μm line (T. Hashimoto et al. 2019; Y. Sugahara et al. 2021). With the estimated [N II] 205 μm line luminosity assuming $n_{\rm e} = 200\,\mathrm{cm^{-3}}$, we find a 3$\sigma$ lower limit of $f^{\rm PDR}_{\rm [C\,II]} > 0.94$ for $R_{\rm ion} = 3.6$, respectively. These $f^{\rm PDR}_{\rm [C\,II]}$ are thus similarly high as our [N II] 205 μm observed samples. Even using the large value of $R_{\rm ion} = 5.7$, we find $f^{\rm PDR}_{\rm [C\,II]} > 0.87$, >0.93, >0.74, and >0.91 for REBELS-38, A1689-zD1, REBELS-25, and B14-65666, respectively.

These inferred PDR fractions of [C II] are high $f^{\rm PDR}_{\rm [CII]}$ compared with those of lower-redshift star-forming galaxies in a similar IR luminosity range and higher than those explained by ionized gas-dominated emissions (left panel of Figure 2).

Previous studies of local IR luminous galaxies find that the dust temperature and the $f^{\rm PDR}_{\rm [CII]}$ correlate well

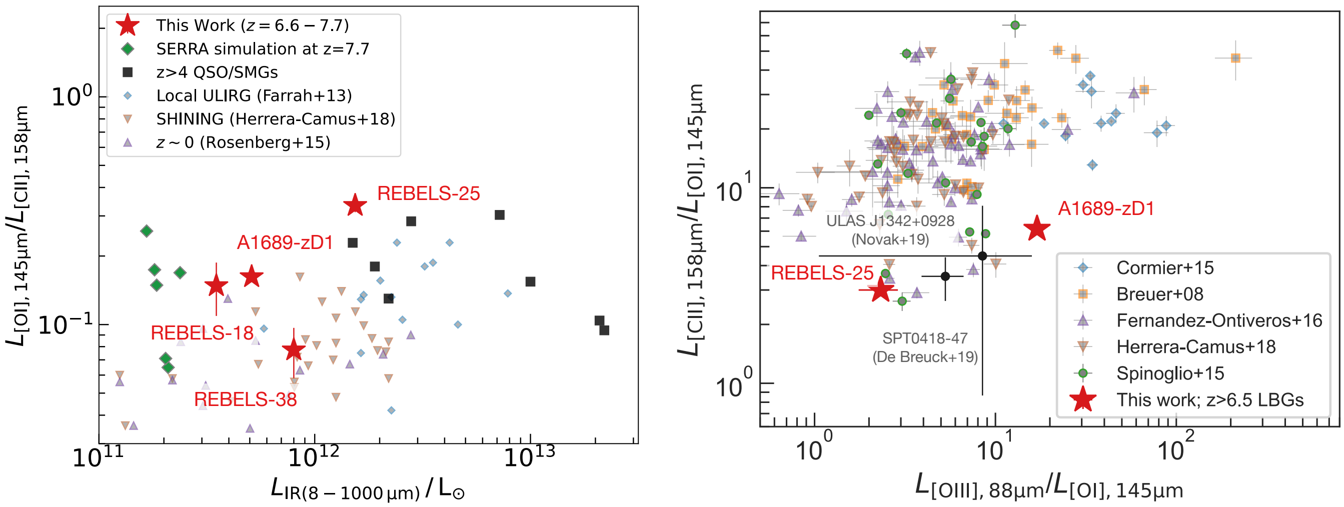

Figure 3. Left panel: [O I] 145 μm over [C II] 158 μm emission line luminosity vs. IR luminosity for local and high-redshift galaxies and AGNs. Blue squares are from C. De Breuck et al. (2019), J. Yang et al. (2019), J. Li et al. (2020), M. M. Lee et al. (2021), R. A. Meyer et al. (2022), simulated results for $z \sim 6$ galaxies are from (A. Lupi & S. Bovino 2020), and $z \sim 0$ galaxies are from D. Farrah et al. (2013), L. Spinoglio et al. (2015), R. Herrera-Camus et al. (2018), M. J. F. Rosenberg et al. (2015). This work (red large stars) expanded [O I] emission line observations of high-redshift galaxies toward the lower IR luminosity range. The results show that the [O I]/[C II] ratio of high-redshift galaxies has similar values to those of local galaxies, but tends to distribute at around the highest edge of the distribution. Right panel: [C II] 158 μm over [O I] 145 μm line luminosity vs. [O III] 88 μm over [O I] 145 μm line luminosity for local- and high-redshift galaxies and AGNs. Seyferts (L. Spinoglio et al. 2015), local AGNs (J. A. Fernández-Ontiveros et al. 2016), SHINING Survey (R. Herrera-Camus et al. 2018), local dwarf galaxies (D. Cormier et al. 2015), local galaxies and Seyferts (J. R. Brauher et al. 2008). High-redshift galaxies and AGNs are from M. Novak et al. (2019) and C. De Breuck et al. (2019).

(e.g., S. Malhotra et al. 2001; T. Díaz-Santos et al. 2017). Our target galaxies are consistent with the correlation found in T. Díaz-Santos et al. (2017) except for the fact that most of the high-redshift and high-T_d galaxies studied here have saturated $f^{PDR}_{[CII]}$ (right panel of Figure 2). T. Díaz-Santos et al. (2017) discussed that the correlation is due to the increase of the gas density in the star-forming region, which result in the increase of dust temperatures, in turn, which enhance the collisional de-excitation or the thermalization of [C II] and makes [C II] 158 μm emission faint especially in ionized region where the critical density of [C II] 158 μm emission is much lower than that in the neutral gas.[29] As a result, the high-density and high-temperature environment of ionized gas would make their contribution to the total [C II] 158 μm luminosity low.

On the other hand, recent studies find an increase in dust temperature as a function of the redshift for normal star-forming galaxies (e.g., C. Schreiber et al. 2018; A. L. Faisst et al. 2020; L. Sommovigo et al. 2022). These studies find that the typical dust temperature of star-forming galaxies at $z \sim 6-7$ to be $T_d \sim 40-60$ K. If the correlation of $f^{PDR}_{[C\,II]}$ and T_d exist for the $z \gtrsim 6$ galaxies and the dust temperature of star-forming galaxies systematically increase as a function of the redshift, the high-redshift star-forming galaxies should have very high or saturated $f^{PDR}_{[C\,II]}$ by combining these two correlations. Our findings of the high $f^{PDR}_{[C\,II]}$ from our target galaxies are consistent with the scenario in which high-redshift galaxies have the high $f^{PDR}_{[C\,II]}$ due to high gas densities and/or high dust temperatures.

These features show that [C II] 158 μm emission lines from star-forming galaxies in the EoR are more dominated by PDR regions compared to lower-redshift galaxies, as also suggested by K. E. Heintz et al. (2022, 2023b). Thus, we conclude that the origin of [C II] 158 μm emission lines of these star-forming galaxies studied here is warm neutral ISM phases associated with PDRs and CO-dark molecular gas layers. This is in line with simulations (e.g., A. Pallottini et al. 2017) and theoretical predictions (e.g., L. Vallini et al. 2017; A. Ferrara et al. 2019). These results indicate that [C II] 158 μm emission is an excellent tracer of neutral ISM.

We hereafter treat all the [C II] emissions from our targets are all come from their neutral ISM phases as mentioned above, and no corrections are applied to remove the contribution from H II regions when studying the line ratios between [O I] 145 μm emission line luminosity in the following sections.

5.2. ISM Properties

5.2.1. CLOUDY Settings and Grids

To analyze the neutral gas conditions of our sample, we used CLOUDY (version 17.03; G. J. Ferland et al. 2017) with the observed ratios of fine structure lines. In this analysis, we focus on modeling emission only from neutral gas (i.e., PDR and molecular gas), and we treat [C II] 158 μm emission lines fully arising from neutral gas as we find in Section 5.1. To make models of neutral gas emission using CLOUDY, we removed ionizing photons from impinging radiation fields.[30]

We fixed the impinging radiation to blackbody radiation with a temperature of $T = 50{,}000$ K by setting `blackbody 5e4 K` in the CLOUDY input, following previous studies (A. Pensabene et al. 2021; R. Decarli et al. 2023). The FUV radiation field intensity was defined using Habing flux in the unit of G_0, where 1 G_0 corresponds to 1.6×10^{-3} erg s^{-1} cm^{-2} over $6 < h\nu < 13.6$ eV (H. J. Habing 1968). We then made a

[29] The critical density of [C II] 158 μm emission is $\sim$50 cm^{-3} and $\sim 3 \times 10^3$ cm^{-3} when the collision pair is the electron and the hydrogen atom/molecule, respectively (e.g., G. J. Stacey et al. 2010; C. L. Carilli & F. Walter 2013).

[30] We allowed the ionizing radiation to be fully absorbed by a large column of gas (N(H) = 10^{24} cm^{-2}) without any leakage using the CLOUDY input of `extinguish by 24 leakage=0`.

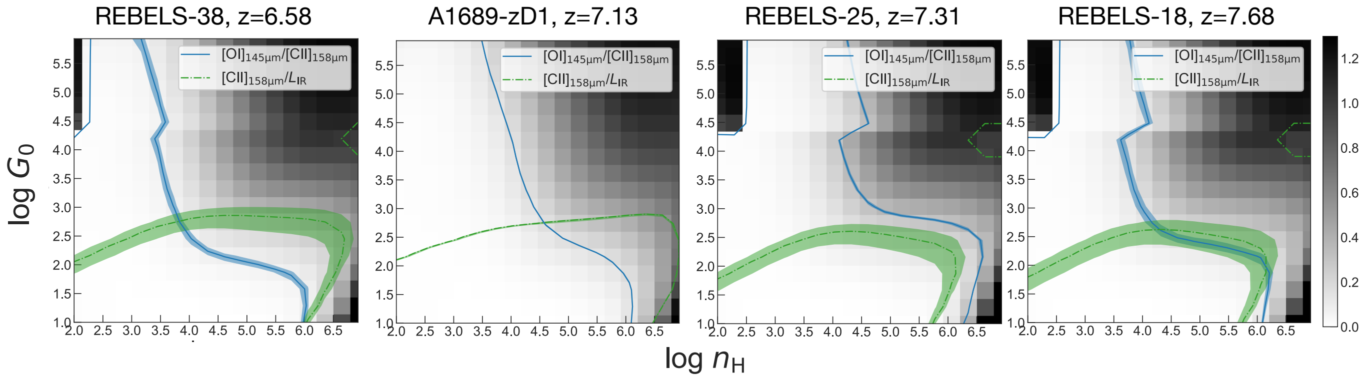

Figure 4. Grid of hydrogen gas density ($n_{\rm H}$ [cm^{-3}]) vs. interstellar radiation field (G_0) calculated using CLOUDY (G. J. Ferland et al. 2017), assuming gas-phase metallicity recently estimated for each galaxy from JWST observations and total gas column density of $\log(N_{\rm H}\ {\rm cm}^{-2}) = 23$. Background images show [O I] 145 μm/[C II] 158 μm intensity ratio calculated in each grid. The observed luminosity ratios for each galaxy are plotted by solid and dashed lines, and 1σ uncertainties are shown by bands. While the estimated FUV field strengths are similar for these galaxies, with $G_0 \sim 10^{2.5}$–$10^{3.0}$, and PDR gas densities are high with $n_{\rm PDR} \sim 10^{3.5}$–$10^{6}$ cm^{-3}.

grid of G_0 ranging $1 < \log G_0 < 6$, and $\log G_0$ is spaced by 0.29 dex. Cosmic rays are added as a background, which works for the ionization balance in deep neutral-molecular gas regions. We used the CLOUDY's default setting by using the command: `cosmic rays, background`. We used the plane-parallel geometry with a constant hydrogen density by setting `constant density`. The elemental and the dust grain abundance are adopted using CLOUDY's default set for ISM by setting `abundance ISM`. The polycyclic aromatic hydrocarbons (PAHs) abundance is then set by using `grains PAH`. The grain and gas metallicity is scaled to values based on the oxygen abundance measurements by recent JWST observations; $12 + \log({\rm O/H}) = 8.45$, 8.05, 8.63, and 8.50 for REBELS-38, A1689-zD1, REBELS-25, and REBELS-18, respectively (L. E. Rowland et al. 2026 and Carmen Blanco-Prieto; private communications). Finally, we set a stopping criterion of reaching a gas column density of $\log(N_{\rm H}/{\rm cm}^{-2}) = 23$. We executed all the CLOUDY runs until it converges using `iterate to converge`. The neutral gas density ranges $2 < \log n_{\rm H}/{\rm cm}^3 < 7$ spaced by 0.29 dex.

With the above CLOUDY setups, we made a grid of emission line models by varying hydrogen density $n_{\rm H}\,{\rm cm}^{-3}$ and radiation field strength. We then calculated emission ratios of [C II]/$L_{\rm IR}$ and [C II]/[O I] for all $n_{\rm H}\,{\rm cm}^{-3}$ and FUV radiation field strength.[31]

5.2.2. Gas Densities and FUV Field Strengths of Star-forming Galaxies in the EoR

Figure 4 shows our results of the CLOUDY modelings with measured [O I] 145 μm/[C II] 158 μm and [C II]/$L_{\rm IR}$ emission ratios. All galaxies except for REBELS-25 have solutions of G_0 and $n_{\rm H}$ that explain the observed line ratios. We find that radiation field strengths have similar values, ranging around $\log G_0 \sim 2.5 - 3.0$. This range of radiation field strength is a factor of a few to up to an order of magnitude lower than those found in high-redshift SMGs or quasars (see Figure 5; M. S. Bothwell et al. 2017; C. De Breuck et al. 2019; M. Novak et al. 2019; A. Pensabene et al. 2021; R. A. Meyer et al. 2022). On the other hand, the gas densities range $\log n_{\rm H}\ {\rm cm}^{-3} \sim 3.5$ to $\sim$6 that are $\times$10 to $\times$1000 higher than those of local main-sequence galaxies and that are similar to those of local major mergers, high-redshift starbursts, or SMGs (e.g., T. M. Hughes et al. 2017; V. Markov et al. 2022). Overall, compared with high-redshift ($z \sim 4$–6) SMGs, our target star-forming galaxies in the EoR have a similar range of gas densities and lower FUV radiation field strengths (Figure 5). A scaling argument based on the definitions of G_0 and $n_{\rm H}$ suggests that, for comparable gas cloud densities, systems with lower overall star formation activity can naturally have weaker effective FUV radiation fields. This provides an interpretation of the trend seen in Figure 5. A more quantitative interpretation, including the effects of geometry and the detailed structure of PDRs, can be found in detailed PDR modeling (e.g., M. G. Wolfire et al. 1990).

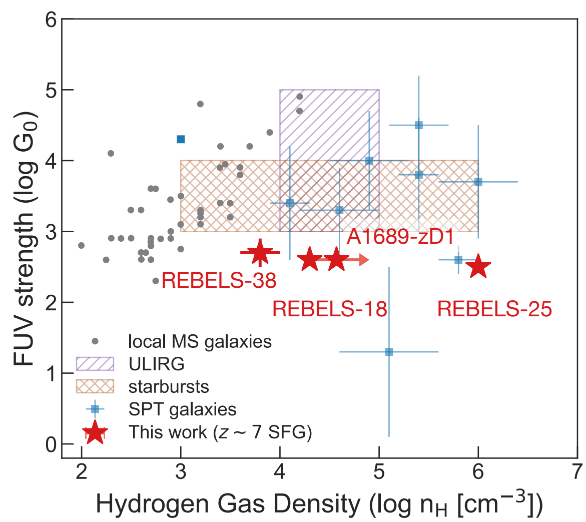

Figure 5. Hydrogen gas density ($n_{\rm H}$) vs. FUV field strength (G_0) of local and high-redshift galaxies. Gray dots show local main-sequence galaxies (S. Malhotra et al. 2001). $n_{\rm PDR}$ and G_0 range of local ULIRGs and starbursts are shown using purple and green hatched squares, respectively (G. J. Stacey et al. 1991; R. I. Davies et al. 2003). Blue squares are $z \sim 4$ dust-obscured starbursts observed as part of the SPT survey (M. S. Bothwell et al. 2017; C. De Breuck et al. 2019). Our target galaxies, [C II] bright star-forming galaxies in the EoR, have higher ($\times\sim$10 to $\times\sim$1000) gas density than local main-sequence galaxies, while UV field strengths are similar to local main-sequence galaxies and lower than those of starbursts.

We note that there would be no clear solution obtained in REBELS-25. The difficulty of explaining REBELS-25's emission line ratios is possibly related to the uncertainty in the gas-phase metallicity of the warm neutral ISM. While the

[31] We publish input files and output grids of our CLOUDY run: https://github.com/yfudamoto/Fudamoto_OI_cloudy.git

metallicity is estimated from ionized gas emission lines observed with JWST (L. E. Rowland et al. 2026) and is assumed to apply to both ionized and neutral phases, we find that adopting this metallicity (12 + log(O/H) = 8.63) does not allow any combination G_0 and n_H to simultaneously reproduce the observed [O I]/[C II] and [C II]/L_{IR} ratios within our CLOUDY model grid (Figure 5).

In contrast, when a lower metallicity (12 + log(O/H) = 8.05) is adopted, the model grid yields a limited region of parameter space in which the observed line ratios can be reproduced, with $G_0 \sim 10^{2.5}$ and $n_H \sim 10^6\,\mathrm{cm}^{-3}$. This suggests that the observed line ratios are reproduced when a lower metallicity is assumed for the neutral ISM traced by [C II] and [O I].

Such a difference between the metallicity of ionized gas and that of the neutral ISM could arise if part of this warm neutral gas is less chemically enriched, for example, due to the presence of inflowing low-metallicity gas. Given these uncertainties, we do not attempt to uniquely determine the physical conditions of REBELS-25, but instead adopt $G_0 \sim 10^{2.5}$ and $n_H \sim 10^{6.5}\,\mathrm{cm}^{-3}$ as representative values consistent with the observed line ratios.

We also note that some of the small uncertainties of G_0 and n_H, especially for the parameters of A1689-zD1, are primarily driven by the high signal-to-noise ratio of the observed line ratios. As a result, the comparison with the model grid sometimes yields tightly constrained parameters when only observational uncertainties are considered. However, these formal errors do not account for systematic uncertainties associated with the adopted single-zone approximation, optical depth, and/or the relative distribution of radiation sources and gas (e.g., N. P. Abel et al. 2007; M. Röllig et al. 2007; T. M. Hughes et al. 2017). Therefore, the true uncertainties on the physical conditions could be larger than the quoted formal errors.

5.3. Hydrogen and Oxygen Mass

5.3.1. Oxygen Mass

In the optically thin limit,[32] the oxygen atom masses of galaxies can be derived using [O I] 145 μm luminosity and the following formula

$$M_O/M_\odot = 6.19 \times 10^{-5}\, Q(T_{ex})\, e^{327\,\mathrm{K}/T_{ex}}\, L'_{[OI]145}, \quad (2)$$

where $Q(T_{ex})$ is the partition function and $Q(T_{ex}) = 5 + 3\,e^{-228\,\mathrm{K}/T_{ex}} + e^{-327\,\mathrm{K}/T_{ex}}$ for the oxygen atom, $L'_{[OI]145}/\mathrm{K\,km\,s^{-1}\,pc^2}$ is the integrated [O I] 145 μm brightness temperature, and T_{ex}/K is the excitation temperature (A. Weiß et al. 2003, 2005; R. A. Meyer et al. 2022).

For the calculation, we assume an excitation temperature of T_{ex} = 100 K, which is a representative gas temperature (T_{gas}) of the line-emitting region in our CLOUDY run ($n_H = 10^{4.5}\,\mathrm{cm}^{-3}$ and $G_0 = 10^{2.7}$). We assume $T_{ex} = T_{gas}$ as a first-order approximation.

We therefore estimated neutral oxygen masses of our targets between $0.4 \times 10^7\,M_\odot$ and $1.6 \times 10^7\,M_\odot$ (Table 4).

We note that if we assume a higher T_{ex}, the estimated atomic oxygen masses become smaller. As an example, $M_{O,150\,K} = 1.8 \times 10^6$ assuming T_{ex} = 150 K for REBELS-38. On the other hand, lower T_{ex} results in significantly higher oxygen masses; e.g., $M_{O,50\,K} = 1.0 \times 10^8$ assuming T_{ex} = 50 K for REBELS-38. Thus, there would be a large systemic uncertainty in the estimated atomic oxygen masses from the assumed excitation temperature.

5.3.2. Warm Neutral Gas Masses of EoR Star-forming Galaxies

With the estimated atomic oxygen masses, we estimate hydrogen masses of our target galaxies that share the same volume as the [O I] emitting regions, i.e., the warm atomic gas associated with dense PDR phases. To do this, we used oxygen abundances recently estimated using optical [O III] with Hβ lines from JWST observations (L. E. Rowland et al. 2026; M. Stefanon et al., 2025 in preparation; C. Blanco-Prieto et al., 2025 in preparation). For this purpose, we applied oxygen abundances from JWST observations that were assumed during the CLOUDY calculations.[33] By applying the oxygen abundance to the derived oxygen mass, we find M_H between $0.9 \pm 0.2 \times 10^9\,M_\odot$ and $3.0 \pm 0.2 \times 10^9\,M_\odot$ (Table 4). With the estimated hydrogen mass, we estimate gas mass fractions of $M_H/(M_* + M_H) \sim 0.2-0.4$, which are lower but within the similar ranges recently derived from high-redshift galaxy studies using [C II] 158 μm lines (S. Hailey-Dunsheath et al. 2010; M. Dessauges-Zavadsky et al. 2020; K. E. Heintz et al. 2022; M. Aravena et al. 2024; K. E. Heintz et al. 2024).

S. N. Wilson et al. (2024) reported a tight correlation between [O I] 145 μm emission line luminosities and H I gas masses in $z \sim 2$–6 star-forming galaxies using gamma-ray bursts as a probe, and supported by local galaxy observations and hydro-dynamical simulations. Using the correlation, we find H I gas masses of 3.9×10^9, $1.5 \times 4.14/\mu \times 10^{10}$, 2.3×10^{10}, $6.9 \times 10^9\,M_\odot$ for REBELS-38, A1689-zD1, REBELS-25, and REBELS-18, respectively.

We also compared the estimated hydrogen masses with gas masses estimated using [C II] 158 μm emission lines. To do this comparison, we used the relation found in S. Hailey-Dunsheath et al. (2010), who employed constraints on PDR models to derive the atomic gas mass of a hyperluminous ($L_{IR} \sim 10^{13}\,L_\odot$) starburst galaxy at $z = 1.3$. Using equation (1) of S. Hailey-Dunsheath et al. (2010) and applying an estimated gas density and gas temperature of 100 K, we find the atomic gas masses to be 2.1×10^9, $1.4 \times 10^9 \times (4.14/\mu)$, 2.0×10^9, and 1.4×10^9 for REBELS-38, A1689-zD1, REBELS-25, and REBELS-18, respectively. We also used the correlation found in A. Zanella et al. (2018). From the correlation, we found molecular gas masses of $M_{H_2} = 5.2 \times 10^{10}$, $3.4 \times 10^{10} \times (4.14/\mu)$, 5.0×10^{10}, and $3.3 \times 10^{10}\,M_\odot$ for REBELS-38, A1689-zD1, REBELS-25, and REBELS-38, respectively. The derived gas masses are summarized in Table 5.

These derived gas masses from [O I] and [C II] lines are generally consistent among these methods but the empirically calibrated methods, such as those employed in S. N. Wilson et al. (2024) and A. Zanella et al. (2018), results in a factor of a few times to more than an order of magnitude higher hydrogen masses than those we derived using [O I] 145 μm emission. On the other hand, similar PDR/warm neutral gas analysis employed in S. Hailey-Dunsheath et al. (2010) results in an excellent agreement, even when the emission lines used are

[32] [O I] 145 μm emission is optically thin in a wide range of parameter space (e.g., M. J. Kaufman et al. 1999).

[33] 12 + log(O/H) = 8.45, 8.05, 8.63, and 8.53 for REBELS-38, A1689-zD1, REBELS-25, and REBELS-18, respectively

Table 4
Neutral Gas Properties Estimated by CLOUDY at Excitation Temperature of 150 K for [O I] 145 μm Line and Oxygen Abundances

ID	FUV strength (G_0)	n_H (cm^{-3})	$M_{O,T_{ex}=100\,K}$ ($\times 10^7\, M_\odot$)	$M_{H\_[O\ I]145}$ ($\times 10^9\, M_\odot$)
REBELS-38	$10^{2.8\pm0.2}$	$10^{3.8\pm0.2}$	0.4 ± 0.1	0.9 ± 0.2
A1689-zD1	$10^{2.76\pm0.02}$	$10^{4.57\pm0.03}$	2.3 ± 0.5 × (4.14/μ)	3.0 ± 0.2 × (4.14/μ)
REBELS-25	$\sim10^{2.5}$	$\sim10^{6.5}$	1.6 ± 0.3	2.4 ± 0.5
REBELS-18	$\sim10^{2.6}$	$>10^{4.3}$	0.5 ± 0.1	1.0 ± 0.2

Table 5
Comparison of Gas Mass Estimates Using Different Tracers and Methods

Galaxy (1)	$M_{H\ I\,[O\ I]}$ ($\times 10^9\, M_\odot$) (2)	$M_{H\ I\,[C\ II]}$ ($\times 10^9\, M_\odot$) (3)	$M_{H\ I\,[O\ I]\ (empirical)}$ ($\times 10^9\, M_\odot$) (4)	$M_{H_2\,[C\ II]\ (empirical)}$ ($\times 10^9\, M_\odot$) (5)
REBELS-38	0.9 ± 0.2	2.1 ± 0.2	3.9 ± 0.9	52 ± 5
A1689-zD1	3.0 ± 0.2 × (4.14/μ)	1.4 ± 0.3 × (4.14/μ)	15 ± 4 × (4.14/μ)	34 ± 0.7 × (4.14/μ)
REBELS-25	2.4 ± 0.5	2.0 ± 0.1	23 ± 5	50 ± 3
REBELS-18	1.0 ± 0.2	1.4 ± 0.1	6.9 ± 1.7	33 ± 3

Note. Column (2): hydrogen masses in the warm neutral medium derived from [O I] emission assuming oxygen abundances from JWST spectroscopy. Column (3): from [C II] line using the PDR-based method of S. Hailey-Dunsheath et al. (2010) with $T_{gas} = 100$ K. Column (4): empirical [O I]–H I calibration from S. N. Wilson et al. (2024). Column (5): empirical [C II]–M_{H_2} relation from A. Zanella et al. (2018). For A1689-zD1, values are corrected for lensing magnification μ.

different. Given the relatively large uncertainties of within parameters used (e.g., [C II]-to-M_{H_2} conversion), these estimates might still be consistent. However, these systematic excess more likely to represent a large neutral gas reservoir that cannot be traced directly by [O I] 145 μm and/or [C II] lines, as these arise mainly from the warm neutral gas. In this case, empirical calibrations, such as the one employed in S. N. Wilson et al. (2024), for the case of [O I] 145 μm line, would be required to account for these effects. Larger statistical analysis is thus required to derive the accurate correction to derive total neutral gas masses. Further detailed analysis is, however, beyond the scope of this paper.

6. Conclusion

In this paper, we presented results of multiple FIR emission line observations and analysis of four highly star-forming galaxies in the EoR at $z > 6.5$. These galaxies have SFRs that are ∼2–4× above the main sequence at their redshift, and thus less extreme than previously observed SMGs/QSOs. The target galaxies were selected based on their previous detections of luminous [C II] 158 μm emission lines ($L_{[C\ II]} > 10^9\, L_\odot$). We performed follow-up observations of [O I] 145 μm and [N II] 205 μm emission lines of the target galaxies. As a result of the follow-up ALMA observations and analysis, we find the following:

1. From the [N II] 205 μm emission line observations, we only find nondetections and tentative detections, showing that [N II] 205 μm emission lines are much fainter than [C II] 158 μm emission lines (3σ upper limit of $L_{[C\ II]158}/L_{[N\ II]205} > 21$ to > 87). From these high $L_{[C\ II]158}/L_{[N\ II]205}$ ratios, we estimate the fraction of [C II] 158 μm emission arising from ionized gas and find that the dominant fraction of [C II] 158 μm emission lines arises from neutral gas with $f^{PDR} > 0.74$ to > 0.96 (3σ lower limits). These results confirm that [C II] 158 μm emission is an excellent tracer of the neutral phase of the star-forming gas/ISM.

2. We detect [O I] 145 μm emission lines from all the target galaxies and find [O I] 145 μm/[C II] 158 μm luminosity ratio of 0.08 - 0.33 (median 0.16). These observations mark the first detections of [O I] 145 μm emission lines from [C II]-bright star-forming galaxies in the EoR at $z > 6.5$. These detections demonstrate that [O I] 145 μm observations are feasible for characterizing the neutral gas in larger samples of high-redshift galaxies.

3. Using spectral synthesis calculations of CLOUDY, we model neutral gas conditions of the target galaxies. By calculating FIR emissions in a grid of gas densities and FUV radiation field strengths, we find that the target galaxies have a moderate FUV radiation field strength of $G_0 \sim 10^{2.5}$–$10^{3.0}$. We also find high PDR gas densities of $n_H \sim 10^4$ to $\sim 10^6$ cm^{-3} that span a similar range with high-redshift ($z \sim 4$ −6) SMGs. Overall, the neutral ISM of [C II] bright star-forming galaxies studied here is characterized by having high gas densities and moderately strong FUV radiation fields: a lower G_0 version of high-redshift SMGs. These features suggest that these star-forming galaxies have similar gas density to SMGs but smaller sizes.

4. We estimate neutral atomic oxygen masses using observed [O I] 145 μm emission luminosities. Then, by combining oxygen abundances recently obtained in recent JWST spectroscopy, we derive the mass of neutral hydrogen that resides in the same region as neutral atomic oxygen. The estimated gas mass ratios ($M_H/(M_* + M_H)$) range from 0.2 to 0.4. The derived hydrogen masses are a factor of a few to an order of magnitude smaller than those empirically derived using [C II] 158 μm and [O I] emission lines. However, our results are in excellent agreement with the results obtained from PDR/warm neutral gas analysis using [C II] emission line. These observations and analyses show that directly converting oxygen masses to hydrogen masses using JWST-derived oxygen abundances might be possible. However, the method employed in this study potentially misses neutral gas that is in colder phases, and a more empirically calibrated method might be required to correct for such effects.

The rapid progress of JWST observations opened a new era for galaxy studies in the EoR by finding large numbers of galaxies in the heart of cosmic reionization and by enabling observations of their rest-frame optical wavelength. To fully understand galaxy growth at high redshift, however, observations of neutral gas and cold ISM tracers are essential, and such observations are only possible using millimeter/submillimeter facilities such as ALMA. Through the first detections of [O I] 145 μm from star-forming galaxies in the EoR that are more representative of the typical galaxy population than SMGs or QSOs, our pilot observations demonstrate how multiline observations in FIR wavelength enable our access to gas properties in neutral gas regions. Future surveys at FIR wavelengths, particularly [O I] emission lines, in conjunction with JWST observations, will allow us to analyze multiple phases of gas, stars, and dust directly in high-redshift galaxies.

Acknowledgments

We thank Carmen Blanco-Prieto, Javier Arvarez-Marquez, Luis Colina, and the team of JWST observation (GO-1840) for important discussions about the JWST observations of A1689-zD1. This paper makes use of the following ALMA data: ADS/JAO.ALMA#2022.1.00446.S ALMA is a partnership of ESO (representing its member states), NSF (USA) and NINS (Japan), together with NRC (Canada), MOST and ASIAA (Taiwan), and KASI (Republic of Korea), in cooperation with the Republic of Chile. The Joint ALMA Observatory is operated by ESO, AUI/NRAO, and NAOJ. Y. F., Y.S., and A.K.I. acknowledge support from NAOJ ALMA Scientific Research grant No. 2020-16B. This work was supported by JSPS KAKENHI Grant Nos. JP22K21349 and JP23K13149. P.D. acknowledges support from the NWO grant 016.VIDI.189.162 ("ODIN") and from the European Commission's and University of Groningen's CO-FUND Rosalind Franklin program. H.I. and H.S.B.A. acknowledge support from the NAOJ ALMA Scientific Research Grant Code 2021-19A. H.I. acknowledges support from JSPS KAKENHI grant No. JP19K23462. R.A.A.B. acknowledges support from an STFC Ernest Rutherford Fellowship [grant No. ST/T003596/1]. M.A. is supported by FONDECYT grant No 1252054, and gratefully acknowledges support from ANID Basal Project FB210003 and ANID MILENIO NCN2024_112. S.F. acknowledges the funding from NASA through the NASA Hubble Fellowship grant #HST-HF2-51505.001-A awarded by the Space Telescope Science Institute, which is operated by the Association of Universities for Research in Astronomy, Incorporated, under NASA contract NAS5-26555.

Facilities: ALMA, VISTA, HST.

Software: astropy (Astropy Collaboration et al. 2022), Cloudy (G. J. Ferland et al. 2017).

Appendix A
Gravitational Lens Model of Abell 1689

Within the selected targets, A1689-zD1 is strongly lensed by the foreground galaxy cluster Abell 1689. The magnification factor of A1689-zD1 is presented in D. Watson et al. (2015) using the pioneering mass modeling of the Abell 1689 T. Broadhurst et al. (2005), M. Limousin et al. (2007). Since then, new spectroscopy data have been published, and redshifts of several multiple images are updated (D. Bina et al. 2016). Thus, we reanalyze the mass model of Abell 1689 using the updated multiple image data and an updated lens modeling code.

Using the public code GLAFIC (M. Oguri 2010, 2021), we estimate the mass model of the Abell 1689 cluster using the public multiple image catalogs (D. Coe et al. 2010; A. Ghosh et al. 2023), removing insecure multiple images. Some of the spectroscopic redshifts of the multiple images are obtained using the MUSE observation results (D. Bina et al. 2016). We used 130 multiple images of 40 source galaxies, 14 of which have spectroscopic redshifts. The cluster is modeled with the five Navarro–Frenk–White components with a fast approximation (M. Oguri 2021), cluster galaxies (D. Coe et al. 2010), and external shear, and $m = 3$ and 4 multipole perturbations (M. Oguri 2010). We then run GLAFIC software to find the minimum χ^2 assuming positional errors of $0\farcs8$ for multiple image positions. The relatively large positional errors reflect the fact that Abell 1689 is one of the most massive clusters in the Universe, with a highly complex mass distribution. The rms of differences between observed and model-predicted multiple image positions is $0\farcs64$ for the best-fitting model.

From the updated mass model, we find a magnification factor for A1689-zD1 to be $\mu = 4.14 \pm 0.36$, which is smaller than that previously reported (e.g., $\mu = 9.3$; T. Broadhurst et al. 2005; D. Watson et al. 2015). The error is calculated using Markov Chain Monte Carlo calculations around the best-fit solutions. Although the magnification factor is relatively uncertain due to the complex structure of the Abell 1689 cluster, we applied a gravitational lensing magnification of $\mu = 4.14$ as our fiducial value throughout this study. The exact value of the magnification factor does not strongly affect our conclusion, as the main focus of this study is line ratios.

Appendix B
Dust Continuum Detections

Here, we summarize images of the dust continuum map of the $\lambda_{\rm rest} = 145\,\mu$m and $\lambda_{\rm rest} = 205\,\mu$m data of the target galaxies. All the dust continua are detected with $>8\sigma$ (Figure 6). Measured fluxes are summarized in Table 3.

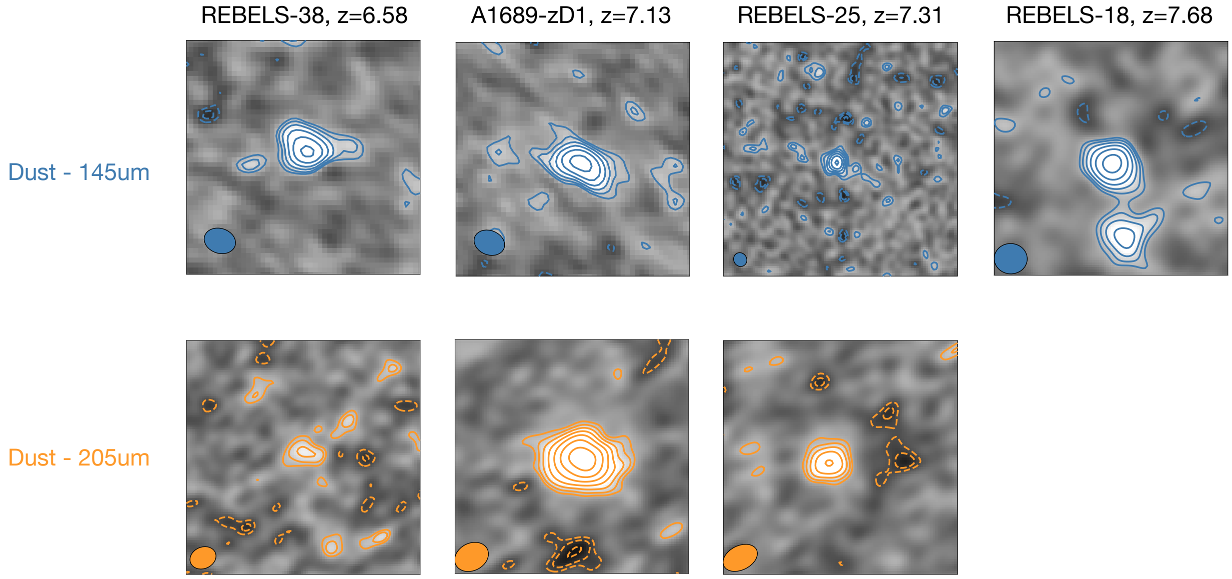

Figure 6. Dust continuum maps at 145 μm (upper panels) and 205 μm (lower panels) for our target galaxies. All maps have a $10'' \times 10''$ size. Solid contours show $2^n\sigma$ significance ($n = 2, 3, 4, \ldots$) and dashed contours show $-1 \times 2^n\sigma$ significance ($n = 2, 3, 4, \ldots$), if they exist. Synthesized beam FWHMs are shown in the lower left corner of the plots. All continuum maps show significant (>4.5σ) detections of dust continua. Measured fluxes are listed in Table 3. The off-center detection in the 145 μm dust image of REBELS-18 is a foreground galaxy with an estimated redshift of $z_{\rm ph} = 3.1$ found in the COSMOS2020 catalog (J. R. Weaver et al. 2023).

ORCID iDs

Yoshinobu Fudamoto https://orcid.org/0000-0001-7440-8832
Akio K. Inoue https://orcid.org/0000-0002-7779-8677
Rychard Bouwens https://orcid.org/0000-0002-4989-2471
Hanae Inami https://orcid.org/0000-0003-4268-0393
Renske Smit https://orcid.org/0000-0001-8034-7802
Daniel P. Stark https://orcid.org/0000-0001-6106-5172
Manuel Aravena https://orcid.org/0000-0002-6290-3198
Andrea Pallottini https://orcid.org/0000-0002-7129-5761
Takuya Hashimoto https://orcid.org/0000-0002-0898-4038
Masamune Oguri https://orcid.org/0000-0003-3484-399X
Hiddo Algera https://orcid.org/0000-0002-4205-9567
Rebecca A. A. Bowler https://orcid.org/0000-0003-3917-1678
Elisabete da Cunha https://orcid.org/0000-0001-9759-4797
Pratika Dayal https://orcid.org/0000-0001-8460-1564
Andrea Ferrara https://orcid.org/0000-0002-9400-7312
Seiji Fujimoto https://orcid.org/0000-0001-7201-5066
Kasper E. Heintz https://orcid.org/0000-0002-9389-7413
Alexander P. S. Hygate https://orcid.org/0000-0002-6488-471X
Ivana F. van Leeuwen https://orcid.org/0009-0005-6803-6805
Ilse De Looze https://orcid.org/0000-0001-9419-6355
Lucie E. Rowland https://orcid.org/0009-0009-2671-4160
Mauro Stefanon https://orcid.org/0000-0001-7768-5309
Yuma Sugahara https://orcid.org/0000-0001-6958-7856
Joris Witstok https://orcid.org/0000-0002-7595-121X
Paul P. van der Werf https://orcid.org/0000-0001-5434-5942

References

Abel, N. P., Dudley, C., Fischer, J., Satyapal, S., & van Hoof, P. A. M. 2009, ApJ, 701, 1147
Abel, N. P., Sarma, A. P., Troland, T. H., & Ferland, G. J. 2007, ApJ, 662, 1024
Akins, H. B., Fujimoto, S., Finlator, K., et al. 2022, ApJ, 934, 64
Algera, H. S. B., Inami, H., De Looze, I., et al. 2024, MNRAS, 533, 3098
Algera, H. S. B., Inami, H., Sommovigo, L., et al. 2023, MNRAS,
Aravena, M., Heintz, K. E., Dessauges-Zavadsky, M., et al. 2024, A&A, 682, A24
Astropy Collaboration, Price-Whelan, A. M., Lim, P. L., et al. 2022, ApJ, 935, 167
Bakx, T. J. L. C., Sommovigo, L., Carniani, S., et al. 2021, MNRAS, 508, L58
Béthermin, M., De Breuck, C., Gullberg, B., et al. 2016, A&A, 586, L7
Bina, D., Pelló, R., Richard, J., et al. 2016, A&A, 590, A14
Bisbas, T. G., Tan, J. C., & Tanaka, K. E. I. 2021, MNRAS, 502, 2701
Bothwell, M. S., Aguirre, J. E., Aravena, M., et al. 2017, MNRAS, 466, 2825
Bouwens, R. J., Illingworth, G. D., Oesch, P. A., et al. 2015, ApJ, 803, 34
Bouwens, R. J., Smit, R., Schouws, S., et al. 2022, ApJ, 931, 160
Bradley, L. D., Bouwens, R. J., Ford, H. C., et al. 2008, ApJ, 678, 647
Brauher, J. R., Dale, D. A., & Helou, G. 2008, ApJS, 178, 280
Broadhurst, T., Benítez, N., Coe, D., et al. 2005, ApJ, 621, 53
Cameron, A. J., Saxena, A., Bunker, A. J., et al. 2023, A&A, 677, A115
Carilli, C. L., & Walter, F. 2013, ARA&A, 51, 105
Carniani, S., Ferrara, A., Maiolino, R., et al. 2020, MNRAS, 499, 5136
Carniani, S., Hainline, K., D'Eugenio, F., et al. 2024, Natur, 633, 318
Cathey, J., Gonzalez, A. H., Lower, S., et al. 2024, ApJ, 967, 11
Chabrier, G. 2003, PASP, 115, 763
Coe, D., Benítez, N., Broadhurst, T., & Moustakas, L. A. 2010, ApJ, 723, 1678
Cormier, D., Madden, S. C., Lebouteiller, V., et al. 2015, A&A, 578, A53
Croxall, K. V., Smith, J. D., Pellegrini, E., et al. 2017, ApJ, 845, 96
Cunningham, D. J. M., Chapman, S. C., Aravena, M., et al. 2020, MNRAS, 494, 4090
Davies, R. I., Sternberg, A., Lehnert, M., & Tacconi-Garman, L. E. 2003, ApJ, 597, 907
Dayal, P., & Ferrara, A. 2018, PhR, 780, 1
De Breuck, C., Weiß, A., Béthermin, M., et al. 2019, A&A, 631, A167
Decarli, R., Pensabene, A., Diaz-Santos, T., et al. 2023, A&A, 673, A157
Decarli, R., Walter, F., Carilli, C., et al. 2014, ApJL, 782, L17
Dessauges-Zavadsky, M., Ginolfi, M., Pozzi, F., et al. 2020, A&A, 643, A5
Díaz-Santos, T., Armus, L., Charmandaris, V., et al. 2017, ApJ, 846, 32
Faisst, A. L., Fudamoto, Y., Oesch, P. A., et al. 2020, MNRAS, 498, 4192
Farrah, D., Lebouteiller, V., Spoon, H. W. W., et al. 2013, ApJ, 776, 38
Ferland, G. J., Chatzikos, M., Guzmán, F., et al. 2017, RMxAA, 53, 385
Ferland, G. J., Korista, K. T., Verner, D. A., et al. 1998, PASP, 110, 761
Fernández Aranda, R., Díaz Santos, T., Hatziminaoglou, E., et al. 2024, A&A, 682, A166
Fernández-Ontiveros, J. A., Spinoglio, L., Pereira-Santaella, M., et al. 2016, ApJS, 226, 19
Ferrara, A., Vallini, L., Pallottini, A., et al. 2019, MNRAS, 489, 1

Finkelstein, S. L., Bagley, M. B., Ferguson, H. C., et al. 2023, ApJL, 946, L13
Fischer, J., Sturm, E., González-Alfonso, E., et al. 2010, A&A, 518, L41
Fudamoto, Y., Inoue, A. K., & Sugahara, Y. 2023, MNRAS, 521, 2962
Fujimoto, S., Arrabal Haro, P., Dickinson, M., et al. 2023, ApJL, 949, L25
Fujimoto, S., Ouchi, M., Nakajima, K., et al. 2024, ApJ, 964, 146
Ghosh, A., Adams, D., Williams, L. L. R., et al. 2023, MNRAS, 525, 2519
Habing, H. J. 1968, BAN, 19, 421
Hailey-Dunsheath, S., Nikola, T., Stacey, G. J., et al. 2010, ApJL, 714, L162
Harikane, Y., Ouchi, M., Inoue, A. K., et al. 2020, ApJ, 896, 93
Harikane, Y., Ouchi, M., Oguri, M., et al. 2023, ApJS, 265, 5
Hashimoto, T., Inoue, A. K., Mawatari, K., et al. 2019, PASJ, 71, 71
Heintz, K. E., Oesch, P. A., Aravena, M., et al. 2022, ApJL, 934, L27
Heintz, K. E., Giménez-Arteaga, C., Fujimoto, S., et al. 2023a, ApJL, 944, L30
Heintz, K. E., Shapley, A. E., Sanders, R. L., et al. 2023b, A&A, 678, A30
Heintz, K. E., Watson, D., Brammer, G., et al. 2024, Sci, 384, 890
Herrera-Camus, R., Sturm, E., Graciá-Carpio, J., et al. 2018, ApJ, 861, 94
Hodge, J. A., & da Cunha, E. 2020, RSOS, 7, 200556
Hollenbach, D. J., & Tielens, A. G. G. M. 1999, RvMP, 71, 173
Hughes, T. M., Ibar, E., Villanueva, V., et al. 2017, A&A, 602, A49
Hunter, D. A., Elmegreen, B. G., & Madden, S. C. 2024, ARA&A, 62, 113
Hygate, A. P. S., Hodge, J. A., da Cunha, E., et al. 2023, MNRAS, 524, 1775
Inami, H., Algera, H. S. B., Schouws, S., et al. 2022, MNRAS, 515, 3126
Inoue, A. K., Hashimoto, T., Chihara, H., & Koike, C. 2020, MNRAS, 495, 1577
Kaufman, M. J., Wolfire, M. G., Hollenbach, D. J., & Luhman, M. L. 1999, ApJ, 527, 795
Killi, M., Watson, D., Fujimoto, S., et al. 2023, MNRAS, 521, 2526
Lebouteiller, V., Cormier, D., Madden, S. C., et al. 2019, A&A, 632, A106
Lee, M. M., Nagao, T., De Breuck, C., et al. 2021, ApJ, 913, 41
Li, J., Wang, R., Cox, P., et al. 2020, ApJ, 900, 131
Limousin, M., Richard, J., Jullo, E., et al. 2007, ApJ, 668, 643
Litke, K. C., Marrone, D. P., Aravena, M., et al. 2023, ApJ, 949, 87
Lupi, A., & Bovino, S. 2020, MNRAS, 492, 2818
Madau, P., & Dickinson, M. 2014, ARA&A, 52, 415
Madden, S. C., Cormier, D., Hony, S., et al. 2020, A&A, 643, A141
Malhotra, S., Kaufman, M. J., Hollenbach, D., et al. 2001, ApJ, 561, 766
Markov, V., Carniani, S., Vallini, L., et al. 2022, A&A, 663, A172
McCracken, H. J., Milvang-Jensen, B., Dunlop, J., et al. 2012, A&A, 544, A156
McKee, C. F., & Ostriker, J. P. 1977, ApJ, 218, 148
Meyer, R. A., Walter, F., Cicone, C., et al. 2022, ApJ, 927, 152
Naidu, R. P., Oesch, P. A., van Dokkum, P., et al. 2022, ApJL, 940, L14
Novak, M., Bañados, E., Decarli, R., et al. 2019, ApJ, 881, 63
Novak, M., Venemans, B. P., Walter, F., et al. 2020, ApJ, 904, 131
Oberst, T. E., Parshley, S. C., Nikola, T., et al. 2011, ApJ, 739, 100
Oesch, P. A., Brammer, G., Naidu, R. P., et al. 2023, MNRAS, 525, 2864
Oesch, P. A., Bouwens, R. J., Illingworth, G. D., Labbé, I., & Stefanon, M. 2018, ApJ, 855, 105
Oguri, M. 2010, PASJ, 62, 1017
Oguri, M. 2021, PASP, 133, 074504
Osterbrock, D. E., & Ferland, G. J. 2006, in Astrophysics of Gaseous Nebulae and Active Galactic Nuclei ads, ed. D.E. Osterbrock & G.J. Ferland (Univ. Science Books)
Pallottini, A., Ferrara, A., Bovino, S., et al. 2017, MNRAS, 471, 4128
Pavesi, R., Riechers, D. A., Faisst, A. L., Stacey, G. J., & Capak, P. L. 2019, ApJ, 882, 168
Pavesi, R., Riechers, D. A., Capak, P. L., et al. 2016, ApJ, 832, 151
Peng, B., Vishwas, A., Stacey, G., et al. 2023, ApJL, 944, L36
Pensabene, A., Decarli, R., Bañados, E., et al. 2021, A&A, 652, A66
Pound, M. W., & Wolfire, M. G. 2023, AJAJ, 165, 25
Rieke, M. J., Robertson, B., Tacchella, S., et al. 2023, ApJS, 269, 16
Robertson, B., Johnson, B. D., Tacchella, S., et al. 2024, ApJ, 970, 31
Robertson, B. E. 2022, ARA&A, 60, 121
Röllig, M., Abel, N. P., Bell, T., et al. 2007, A&A, 467, 187
Rosenberg, M. J. F., van der Werf, P. P., Aalto, S., et al. 2015, ApJ, 801, 72
Rowland, L. E., Hodge, J., Bouwens, R., et al. 2024, MNRAS, 535, 2068
Rowland, L. E., Stefanon, M., Bouwens, R., et al. 2026, MNRAS, 546, staf2023
Schaerer, D., Ginolfi, M., Béthermin, M., et al. 2020, A&A, 643, A3
Schouws, S., Bouwens, R., Smit, R., et al. 2023, ApJ, 954, 103
Schouws, S., Bouwens, R. J., Algera, H., et al. 2025, arXiv:2502.01610
Schouws, S., Stefanon, M., Bouwens, R., et al. 2022, ApJ, 928, 31
Schreiber, C., Elbaz, D., Pannella, M., et al. 2018, A&A, 609, A30
Schreiber, C., Glazebrook, K., Papovich, C., et al. 2021, A&A, 650, C2
Schreiber, C., Pannella, M., Elbaz, D., et al. 2015, A&A, 575, A74
Scoville, N., Sheth, K., Aussel, H., et al. 2016, ApJ, 820, 83
Smit, R., Bouwens, R. J., Carniani, S., et al. 2018, Natur, 553, 178
Solomon, P. M., & Vanden Bout, P. A. 2005, ARA&A, 43, 677
Sommovigo, L., Ferrara, A., Pallottini, A., et al. 2022, MNRAS, 513, 3122
Spinoglio, L., Pereira-Santaella, M., Dasyra, K. M., et al. 2015, ApJ, 799, 21
Stacey, G. J., Geis, N., Genzel, R., et al. 1991, ApJ, 373, 423
Stacey, G. J., Hailey-Dunsheath, S., Ferkinhoff, C., et al. 2010, ApJ, 724, 957
Sugahara, Y., Inoue, A. K., Fudamoto, Y., et al. 2022, ApJ, 935, 119
Sugahara, Y., Inoue, A. K., Hashimoto, T., et al. 2021, ApJ, 923, 5
The CASA Team, Bean, B., Bhatnagar, S., et al. 2022, PASP, 134, 114501
Tielens, A. G. G. M., & Hollenbach, D. 1985, ApJ, 291, 722
Topping, M. W., Stark, D. P., Endsley, R., et al. 2022, MNRAS, 516, 975
Vallini, L., Ferrara, A., Pallottini, A., Carniani, S., & Gallerani, S. 2021, MNRAS, 505, 5543
Vallini, L., Ferrara, A., Pallottini, A., & Gallerani, S. 2017, MNRAS, 467, 1300
Vallini, L., Witstok, J., Sommovigo, L., et al. 2024, MNRAS, 527, 10
Walter, F., Weiß, A., Downes, D., Decarli, R., & Henkel, C. 2011, ApJ, 730, 18
Wang, B., Leja, J., Labbé, I., et al. 2024, ApJS, 270, 12
Watson, D., Christensen, L., Knudsen, K. K., et al. 2015, Natur, 519, 327
Weaver, J. R., Davidzon, I., Toft, S., et al. 2023, A&A, 677, A184
Weiß, A., Henkel, C., Downes, D., & Walter, F. 2003, A&A, 409, L41
Weiß, A., Walter, F., & Scoville, N. Z. 2005, A&A, 438, 533
Williams, C. C., Alberts, S., Ji, Z., et al. 2024, ApJ, 968, 34
Wilson, S. N., Heintz, K. E., Jakobsson, P., et al. 2024, A&A, 685, A30
Witstok, J., Smit, R., Maiolino, R., et al. 2022, MNRAS, 515, 1751
Wolfire, M. G., Tielens, A. G. G. M., & Hollenbach, D. 1990, ApJ, 358, 116
Wong, Y. H. V., Wang, P., Hashimoto, T., et al. 2022, ApJ, 929, 161
Yang, J., Venemans, B., Wang, F., et al. 2019, ApJ, 880, 153
Zanella, A., Daddi, E., Magdis, G., et al. 2018, MNRAS, 481, 1976